3D PRINTING AND ADDITIVE MANUFACTURING
Volume 00, Number 00, 2023

DOI: 10.1089/3dp.2022.0346

Fatigue and Corrosion Evaluation of L-PBF 316L Stainless Steel Having Undergone a Self-Terminating Etching Process for Surface Finish Improvement

Stephanie Prochaska,[1] Subbarao Raikar,[2] and Owen Hildreth[2]

Abstract

The poor surface finish of as-printed (AP) laser powder bed fusion (L-PBF) 316L stainless steels has detrimental impacts on the resulting fatigue and corrosion performance. One postprocessing method, a self-terminating etching process (STEP), can improve the surface finish of parts up to 76%, but the resulting effects on fatigue life and corrosion reliability remain unknown. This work evaluates the effect of the STEP on the fatigue and corrosion performance of L-PBF 316L. In addition, to determine the influence of changing the microstructures from the as-built condition, specimens having undergone a pre-STEP stress relief (SR + STEP) heat treatment and a pre-STEP solution anneal (SA + STEP) were evaluated. The results showed that a pre-STEP SR resulted in the best Sa roughness, while a pre-STEP SA had the biggest improvement in Sv roughness. Despite Sv roughness being a major indicator of fatigue performance, the coarse grains and internal porosity in the SA specimens resulted in the poorest fatigue performance. The SR + STEP specimens' fatigue lives were 10 × higher than the AP samples under a load of 275 MPa and 2–3 × higher under a 350 MPa load. The SR + STEP specimen also had the best corrosion performance in a sodium chloride electrolyte due to the smoother surface and least remnant surface carbides.

Keywords: fatigue, self-terminating etching process, surface finish, stress relief

Introduction

As-printed (AP) Laser Powder Bed Fusion (L-PBF) Additive Manufactured (AM) metal components are inherently rough and relatively porous compared with their conventionally manufactured counterparts. These defects can significantly impact the fatigue life[1,2] and corrosion responses[3,4] of the parts. In fatigue studies, the failure mechanism changes depending on the amount of load applied. Fatigue failure initiates at internal defects, that is, porosity, when the applied load is high, while surface region defects dominate fatigue failure at low loads.[2]

For L-PBF 316L stainless steel, Solberg et al. found this transition load to be ~275 MPa.[2] Hatami et al. also showed that AP L-PBF 316L stainless steel had lower fatigue strength compared with conventional 316L; however, the L-PBF 316L fatigue strength surpassed that of conventional 316L after surface smoothing through machining.[5]

Component microstructure also affects the fatigue life of conventional and L-PBF 316L stainless steels but is highly dependent on a multitude of other factors, and literature disputes an explicit effect. For example, coarser grains have been shown to increase the fatigue threshold stress intensity factor, but the fatigue endurance limit decreases.[6] Cui et al. showed that AP L-PBF 316L stainless steel has superior fatigue properties to a larger grained wrought 316L due to the AM material's high dislocation density and cellular grain structure impeding the localization of strain and inhibiting crack initiation.[7]

When coupled with internal defects, a smaller grain structure causes a random and disperse initiation of microcracks, impeding formation of stress concentration points.[8] However, coarser grained microstructures have less grain boundary volume to accommodate the movement of dislocations, which can pile up on slip bands and lead to stress concentration points.[9] Lorenzino and Navarro have shown that the fatigue performance of coarser grained materials is

[1]Department of Mechanical Engineering, Materials Science Program, Colorado School of Mines, Golden, Colorado, USA.
[2]Department of Mechanical Engineering, Colorado School of Mines, Golden, Colorado, USA.

less sensitive to surface notches than that of fine-grained materials with the same sized notches.[10]

Meanwhile, surface roughness also impacts corrosion properties.[3,11] Melia et al. found that decreasing the surface roughness of L-PBF 316L stainless steel increases the breakdown potential (E_{bd})—the potential at which the protective passive film breaks down and pitting initiates.[3] Multiple studies of conventional and L-PBF 316L stainless steel focus on various postprocessing methods to improve corrosion properties through surface smoothing. These include both mechanical and chemical processes such as machining,[12] shot or laser peening,[13–16] and chemically accelerated vibratory finishing,[17] among others. Since many of these processes also improve fatigue performance,[18] much of the current work in the field of AM involves investigation of postprocessing methods aimed at improving part surface roughness and, subsequently, fatigue life.

One such method for 316L stainless steel is a self-terminating etching process (STEP), which selectively carburizes the top 100–250 μm of the steel.[19] Then, electrochemical etching removes the sensitized region, resulting in an $\sim$50–75% improvement in Ra surface roughness.[19–21] In addition to producing smoother surfaces, another utility of the STEP is its ability to selectively dissolve support structures, which can be difficult and time-consuming to remove from parts with complex geometries or internal channels.

Substantiating the resulting fatigue and corrosion properties of parts processed through this technique should occur before widespread utilization of the STEP. This article evaluates the effect of the STEP on the fatigue and corrosion performance of L-PBF 316L stainless steel. To assess the additional impact of microstructural changes, specimens underwent either a standard stress relief (SR) or a solution anneal (SA) before the STEP. Other specimens underwent STEP in the AP condition.

The results of this work determined an optimized etching bias for the STEP, providing a >25% improvement in Sv roughness compared with unprocessed material. This optimization results in a 2–3 $\times$ increase in fatigue life at a load of 350 MPa and a >10 $\times$ increase at a 275 MPa load. Corrosion performance was however degraded due to incomplete etching and remnant surface sensitization.

Materials and Methods

Powder characterization

Table 1 shows the chemical composition of the stainless steel 316L powders. 3D Systems, Inc. (Rock Hill, SC) produced the powders, 15.56 μm in size, through vacuum induction melting inert gas atomization. Combustion and inductively coupled plasma mass spectrometry performed the elemental analysis. Powder chemical composition meets the specification for 316L stainless steel alloys.[22]

Sample preparation

Pursuant to ASTM E466,[23] 3D Systems DMP Flex 360 printed standard-sized round axial fatigue test specimens through L-PBF perpendicularly (Z-direction) to the build plate. The gauge length was 16.5 mm with a 5.5 mm diameter. To evaluate microstructure and corrosion properties, the same build printed disks 30 mm in diameter and 7 mm thick parallel (XY-direction) to the build platform. Print parameters for all parts were as follows: 300 W laser power, 750 mm/s scan speed, 100 μm hatch spacing, and 60 μm layer thickness.

This work sought to determine the effect of microstructure on the STEP and, subsequently, on the fatigue performance. One set of fatigue and disk specimens did not undergo any pre-STEP heat treatment and underwent the STEP in the AP condition. To evaluate how a common postbuild SR may affect the STEP, a second set of samples were stress relieved in a Lindberg Blue M tube furnace at 470°C for 5 h followed by a furnace cool. The stress-relieved samples are designated as ''SR.'' To assess the impact of microstructure recrystallization and grain coarsening on the STEP, a third set of samples were SA in the tube furnace at 1060°C for 1 h followed by an ice water quench. All heat treatments were conducted pursuant to ASTM F3184 [24] and AMS 2759 [25] under an argon gas atmosphere.

The STEP involves two processing stages—sensitization and electrochemical etching. All samples were sensitized by first soaking for 20 min in a saturated solution of sodium hexacyanoferrate (II) decahydrate [$Na_4Fe(CN)_6 \cdot 10H_2O$] and deionized (DI) water (18 MΩ, Thermo Scientific Smart2Pure 3 UV/UF). A length of high temperature 309 stainless steel tool wrap was coated with a thin layer of graphite powder, and the samples were thoroughly packed in a 4.2:1 by mass slurry of $Na_4Fe(CN)_6 \cdot 10H_2O$ and DI water, and were wrapped tightly in the tool wrap. The decomposition of $Na_4Fe(CN)_6 \cdot 10H_2O$ produces CN and H_2O vapors; small holes were pierced into the tool wrap to allow for their release.

The package was placed into a DT-22-FL-8-VA Deltech Front Loading Inert Gas Furnace at room temperature. The furnace was purged and filled with argon gas three times. Then, in the dehydration step, the furnace was ramped at 5°C/min to 90°C, 185°C, and 250°C with a dwell time of 40, 60, and 60 min, respectively. Finally, in the sensitization step, the furnace was ramped to 915°C and held at that temperature for 6.5 h. The package with the samples was removed from the furnace and immediately water quenched.

Electrochemical etching bias optimization. The surface finish resulting from the STEP is highly dependent on the applied potential during the electrochemical etching portion of the STEP. The bias applied should be chosen such that the sensitized region is etched while the base metal is unaffected. In previous early studies, a bias of 580 mV_{SHE} optimized the surface roughness of L-PBF 316L stainless steel to an Ra of

Table 1. Chemical Composition of 316L Stainless Steel Powder in wt.% (Balance Fe)

ICP							*Combustion*			
Mn	*P*	*Si*	*Cr*	*Ni*	*Mo*	*Cu*	*N*	*O*	*C*	*S*
1.40	0.010	0.58	17.9	12.83	2.42	0.06	0.07	0.05	0.02	0.010

2.74 μm.[20] A subsequent study closed in on 550 mV_{SHE} as an optimized bias, although the resulting Ra surface roughness averaged 6 μm and intergranular corrosion extended $\sim$10 μm from the surface into the bulk.[21]

The authors' complementary research on the effect of dislocation density on the STEP found that a pre-STEP SR resulted in the best surface roughness when specimens were etched at 540 mV_{SHE}. These differences are attributed to the improved understanding of the underlying process along with increasing the optimization evaluation criteria to include minimizing intergranular corrosion as well as roughness.

This work continues to expand the study. It utilized stress-relieved specimens sensitized at the same time as the fatigue bars. Sensitized specimen disks were mounted in epoxy such that only the face of one side of the disk was exposed. Once the epoxy was cured, specimens were placed into a corrosion cell along with 0.48 M nitric acid and 0.1 M potassium chloride (KCl) in 1 L DI water electrolyte, a 6.35-mm diameter graphite rod counter electrode, and a KCl salt bridge, which ionically connected a silver/silver chloride reference electrode to the electrolyte.

Electrochemical etching (chronoamperometry) was carried out on a Princeton Applied Research Parstat MC potentiostat at applied potentials of 540, 550, 560, 570, and 580 mV_{SHE}; a Zeiss Axio Vert.A1 inverted microscope took optical images of the specimen polished cross-sections, and the surface roughness was measured with a Bruker DektakXT contact profilometer. Six scans with a sampling length of 5600 μm were performed for each specimen. The lateral resolution was 0.062 μm, and stylus load was 3 mg. A short cutoff (λ_s) at 2.5 μm and a long cutoff (λ_c) at 0.8 mm and a Gaussian regression filtered the data. The results showed a decrease in Ra between 540 and 550 mV_{SHE}, but Ra increased significantly at biases >550 mV_{SHE}. Therefore, a second batch of stress-relieved, sensitized specimens was electrochemically etched at 544, 547, 553, and 556 mV_{SHE} for further optimization.

Figure 1a plots the Ra surface roughness against the applied bias and shows an achieved Ra roughness of 2.05 μm

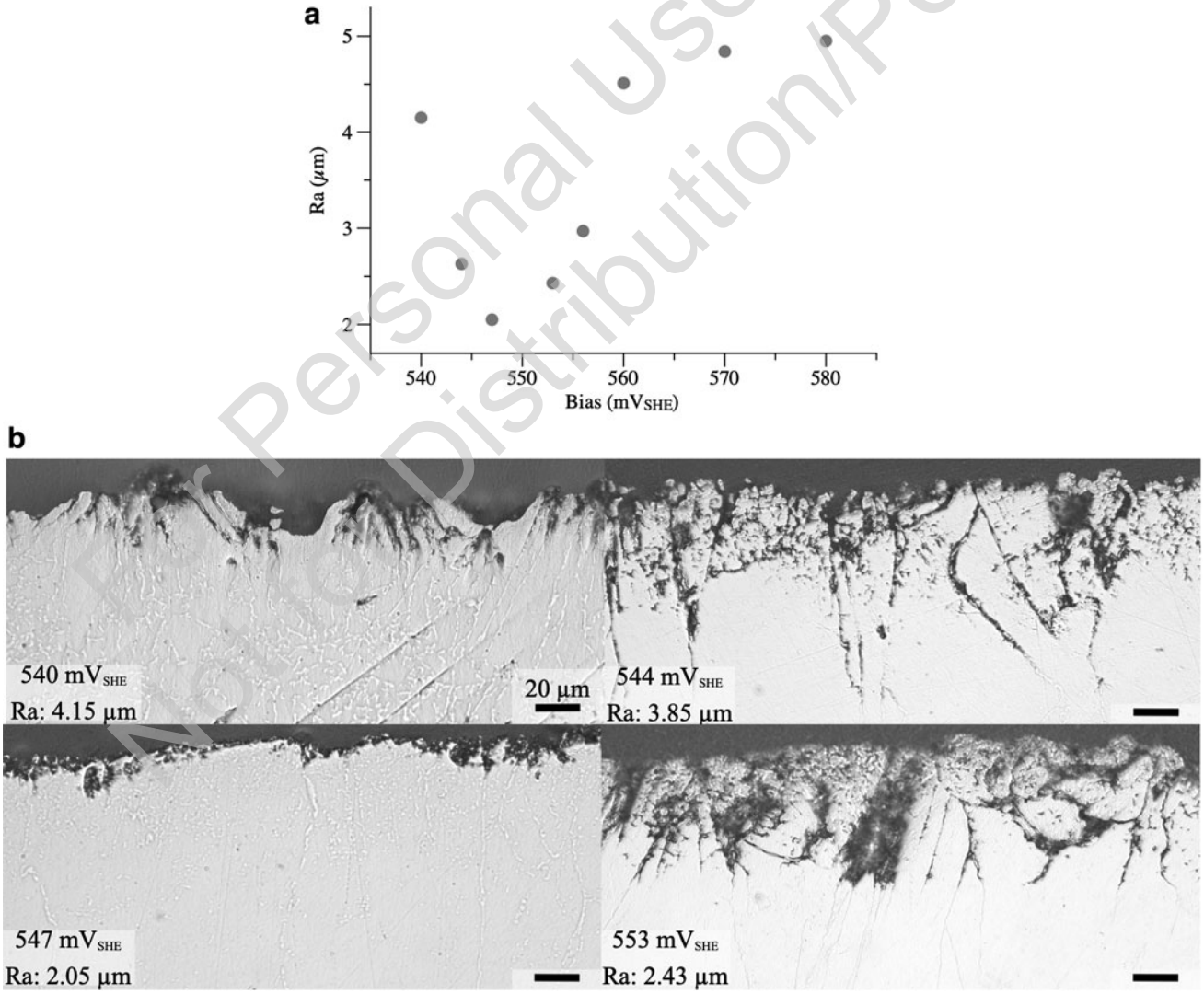

FIG. 1. **(a)** Surface roughness results from the bias study showing a decrease in Ra roughness between 540 and 550 mV_{SHE}. Biases >550 mV_{SHE} resulted in significantly rougher surfaces. **(b)** Optical images of the bias study specimens' polished cross-sections showing varying amounts of near-surface intergranular corrosion. The 547 mV_{SHE} potential was chosen as the optimized bias for this work due to the smallest Ra surface roughness and relatively little intergranular corrosion postetching.

with an applied potential of 547 mV_{SHE}. Further, the cross-sectional micrographs shown in Figure 1b depict the near-surface intergranular corrosion after etching at selected biases. The 547 mV_{SHE} bias had relatively little intergranular corrosion extending into the bulk, and was therefore chosen as the bias to etch the fatigue bars.

To prepare the fatigue bars for electrochemical etching, an exposed length of insulated copper wire was wrapped around the grip portion of one end of the fatigue specimens. The wire and fatigue specimen end were then cold mounted in epoxy (EpoFix, Struers), such that a copper wire lead protruded out of the epoxy. The other grip portion was similarly masked through cold mounting in epoxy. Bars were placed in the corrosion cell as chronoamperometry was initiated at the optimized potential of 547 mV_{SHE} for 48 h. After etching, the epoxy was carefully cut away from the specimens, and they were ultrasonicated in isopropyl alcohol for 60 min. The remaining degradation product was removed from the specimens with a soft bristle brush. Postetching, the fatigue bar gauge length diameters were reduced to an average of 5 mm.

Fatigue testing

An MTS Landmark Model 370.10 servo-hydraulic load frame with vee wedge grips tested the samples' fatigue lives with a maximum stress of 350 MPa. Six samples of each processing condition were evaluated. The load ratio, R, was 0.1, and the cycle frequency was 20 Hz. The dimensions of each specimen were measured individually to ensure application of the correct applied load. Testing was performed at room temperature, and all specimens were tested to failure. Fracture surfaces were imaged with a SEMTech Solutions Model 3300 Field Emission Scanning Electron Microscope at an accelerating voltage of 20 kV and a 23 mm working distance.

Characterization and electrochemistry

An Olympus LEXT 3D Measuring Laser Microscope OLS5100 optical profilometer was used for surface roughness characterization of the fatigue bars. A Gaussian regression was applied with a S filter of 2 μm, and a cylindrical form filter was utilized. The areal roughness parameters quantified were the arithmetic mean height, Sa, and the maximum pit height, Sv.[26]

The disk samples were utilized for microstructure and electrochemical (corrosion) evaluation. To determine the effect STEP on the microstructure, some sample disks were cross-sectioned using a LECO MSX205 sectioning machine and cold mounted in epoxy. Once the epoxy was cured, disk cross-sections were sequentially ground and polished with 180, 320, 400, and 600 grit silicon carbide grinding paper (LECO) and 9, 3, and 1 μm diamond LECO suspensions. To reveal carbides, the polished specimens were electrolytically etched for 80 s under a 6 V potential in a solution of 10 g oxalic acid in 100 mL DI water. Microstructures were imaged with a Zeiss Axio Vert.A1 inverted microscope.

The potentiostat and three-electrode cell components employed for chemical etching were the same used to perform potentiodynamic polarization. The electrolyte was 0.6 M sodium chloride in DI water at room temperature. The sample disks were wrapped with an exposed length of insulated copper wire and mounted in epoxy such that only disk faces were exposed to the electrolyte. Before polarization testing, a stable open circuit potential (OCP) was obtained over a period of 10 h, as depicted in Supplementary Figure S1.

Potentiodynamic polarization was performed at a rate of 1 mV/s from 1 V more negative than the OCP to a vertex of 1.5 V more positive than the OCP. Analysis of the resulting cyclic polarization plots (CPPs) generated values for corrosion potential (E_{corr}), passivation potential (E_{pass}), breakdown potential (E_{bd}), and passive current density (i_{pass}). For reporting relative to a standard hydrogen electrode (SHE), all recorded potentials are offset by +197 mV.

Results and Discussion

As previously described, multiple material characteristics including microstructure and surface roughness influence fatigue and corrosion performance of AM materials. The SR and SA heat treatments alter the parts' dislocation densities and microstructures from the AP condition, and the STEP results therefore differ for each specimen type. The authors' parallel work describes the mechanisms behind these differences, and they will not be repeated here in detail.[27] While the STEP is known to improve the surface roughness of as-built parts, the following results and discussion also describe the influence of the near-surface remnant sensitized material and intergranular corrosion.

Microstructure

The cross-sectional micrographs of the STEP and STEP + SA specimens are shown in Figure 2. The STEP micrographs depict two distinct regions of carbide formation—a dark,

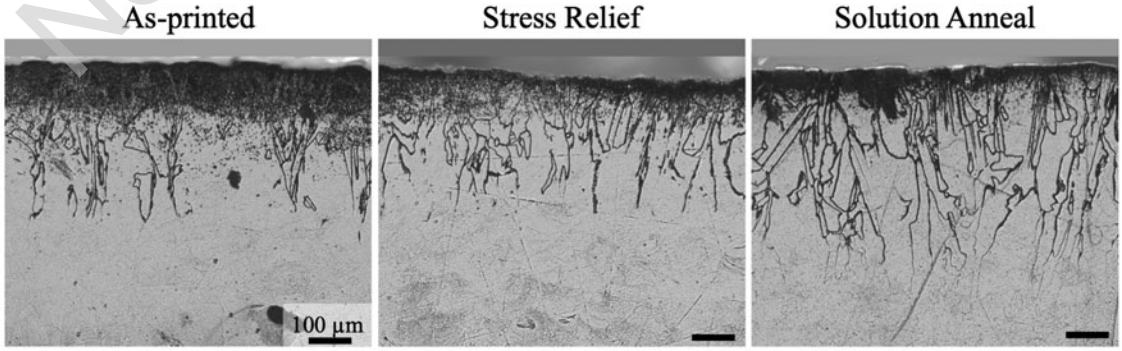

FIG. 2. STEP micrographs depicting the intragranular and intergranular carbide formation regions. STEP, self-terminating etching process.

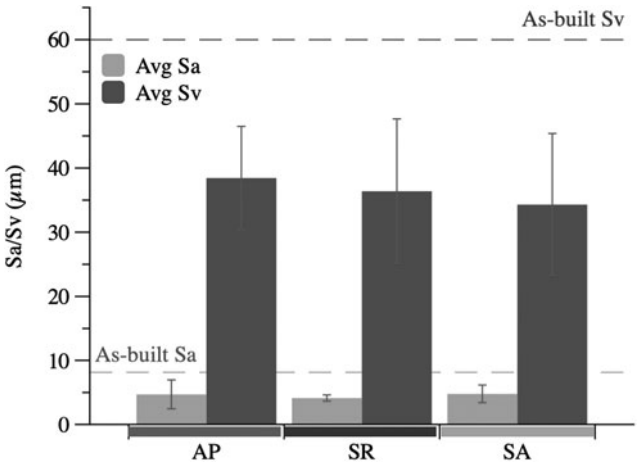

FIG. 3. Average Sa and Sv surface roughness for the fatigue bars evaluated in this study. All specimens had improved Sa and Sv roughnesses compared with the as-built control specimens. The SR produced the best average Sa results, while the SA specimens had, on average, the best Sv results. AP, as-printed; SA, solution anneal; SR, stress relief.

solid intragranular region closest to the surface edge and a region of intergranular carbides. The remnant intragranular region has previously been observed after the STEP and is the deepest in the AP + STEP specimen.[19,21]

The as-built specimens' dislocation densities influence sensitization depth, with higher dislocation density resulting in a shorter intragranular region, since carbon can diffuse along dislocations into the grains rather than predominantly following grain boundaries. Therefore, the sensitized AP specimen's intragranular carbide region is short, and the SA specimen's intragranular region is the longest.

In addition, the material removal during etching terminates along grain boundaries at specific carbide concentrations, and more material is removed in specimens with longer intragranular depths. As such, the AP + STEP specimen has the largest remnant region, while the SR + STEP and SA + STEP specimens have shorter depths of remnant intragranular carbides at the surface. The intergranular carbide depths also differ between the specimens for the same reason as described above and in previous work. In addition, intergranular regions increase with grain coarsening (i.e., as in the SA + STEP specimen) due to limited grain boundary volume.

Profilometry and fatigue testing

A material's endurance limit is highly dependent on the surface condition and residual stress. Lai et al. found the endurance limit of polished L-PBF 316L stainless steel to be ~90 MPa, while a polished specimen that was subsequently stress relieved to resolve residual stress had an endurance limit of 240 MPa.[28] Furthermore, machining, electropolishing, and laser surface remelting to improve surface roughness resulted in a 100–200 MPa improvement in endurance limit compared with as-built stainless steel.[29]

Figure 3 gives the average Sa and Sv roughness for each group of fatigue bars, for comparison, the graph includes Sa and Sv results for an as-built (control) bar. This figure does not include data from one SR + STEP specimen having an uncharacteristically poor surface due to print defects, which significantly skewed the results—the full dataset is provided in Supplementary Figure S2. The STEP resulted in a significant improvement in average Sv roughness compared with the as-built control specimen—an >40% decrease in roughness for all specimens. Average Sv roughness decreased slightly from the AP specimen to the SR specimen, and then to the SA specimen.

The average Sa roughness of the SR + STEP specimens was ~4.1 μm, which is double the average obtained from the bias study. However, specimen geometry (i.e., disk vs. cylindrical bar) and measurement techniques (contact vs. areal) could account for the differences. As previously found, the pre-STEP SR treatment resulted in the smoothest surfaces of all other conditions evaluated, while the coarser grained SA + STEP specimens had the largest average Sa roughness.

In addition to the effects of surface condition, the fatigue strength of 316L stainless steels is directly correlated with tensile strength, with 0.35–0.60 of the tensile strength corresponding to the endurance limit.[30] Due to material limitations, tensile strength could not be directly measured through tensile testing. However, tensile strength, and thus endurance limit, can be approximated through an empirically derived equation (Eq. 1) utilizing the average Rockwell B Hardness (HRB) of the specimens.[31]

$$\textit{Tensile Strength}\,(TS) \approx c_3 \times HRB^3 + c_2 \times HRB^2 + c_1 \times HRB + c_0. \quad (1)$$

In Eq. (1), the constants c_3, c_2, c_1, and c_0 are 0.0006, –0.1216, 9.3502, and –191.89, respectively.[32] Table 2 gives the average measured HRB, the estimated tensile strength, and the endurance limit range for each specimen evaluated in this work. The hardness testing was completed only to estimate endurance limit range, is not intended to represent a comprehensive hardness study of these materials, and is thus not discussed further in this work.

From the calculations, the SR + STEP specimen had the highest estimated tensile strength of 955.0 MPa and

Table 2. Endurance Limit Range Estimated from Rockwell B Hardness Measurements

Specimen	*Average HRB*	*Estimated tensile strength (MPa)*	*Endurance limit (MPa)*	
			0.35TS	*0.6TS*
As-built	100.6	888.6	311.0	533.2
AP + STEP	101.9	918.8	321.6	551.3
SR + STEP	103.5	955.0	334.3	573.0
SA + STEP	102.2	925.6	324.0	555.4

AP, as-printed; HRB, Rockwell B Hardness; SA, solution anneal; SR, stress relief; STEP, self-terminating etching process.

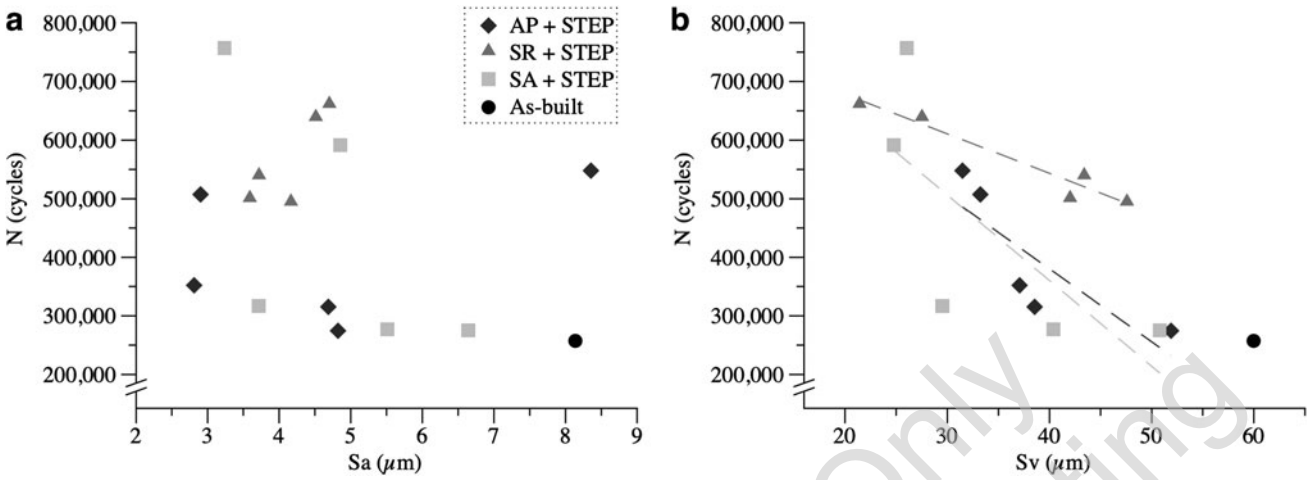

FIG. 4. **(a)** Sa surface roughness and **(b)** Sv surface roughness and the effect on number of cycles to failure. Sv surface roughness had larger influence on fatigue life than Sa surface roughness. The applied load was 350 MPa.

correspondingly the highest endurance limit range of 334.3–573.0 MPa. The SA + STEP and AP + STEP had the next highest tensile strengths, respectively, with the as-built AP control specimen having the lowest tensile strength (888.6 MPa) and lowest endurance limit. These differences trend with the depth of the remnant sensitized region on the specimen samples—the SR having the least and the AP specimen having the most. These endurance limits were verified through testing a few specimens at 275 MPa: the fatigue life of as-built specimens averaged ~760 k cycles, an AP + STEP specimen failed at 1.4 million cycles, and a SR + STEP specimen achieved a runout, exceeding 10 million cycles. The applied load of 350 MPa chosen for the remainder of the testing is within the range of estimated endurance

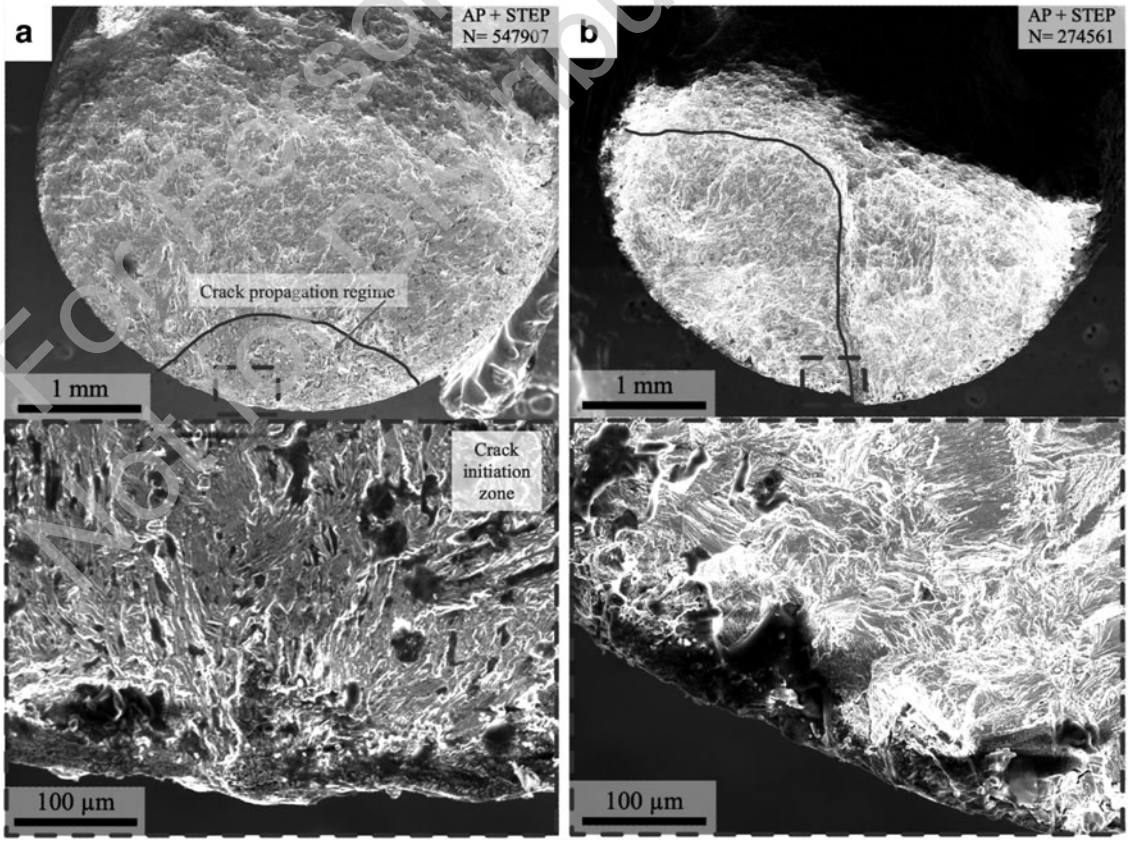

FIG. 5. **(a)** Fracture surface of the best performing ($N = 547{,}907$ cycles) and **(b)** worst performing ($N = 274{,}561$ cycles) AP + STEP fatigue specimens. The specimen in **(a)** exhibited good performance despite a large defect outside of the crack propagation regime. A large surface notch was detrimental to the performance of the specimen in **(b)**.

limits expected for these materials and is nearest to the lower bound of the range; therefore, high cycle fatigue is expected.

Figure 4a and b show the number of cycles to failure for each group of specimens plotted with (a) Sa and (b) Sv profilometry measurements. These plots again do not include the SR + STEP outlier, but the full dataset is provided in Supplementary Figure S3. The results indicate that fatigue life has a much stronger dependence on Sv roughness than Sa, with fatigue life increasing with decreasing Sv.

Further, the SR + STEP provided significantly better fatigue life than the other processing conditions as estimated through the calculations in Table 2. This improvement is likely due to a combination of fine grains, smaller Sa roughness, and fewer remnant surface carbides. Contrarily, despite having the lowest average Sv roughness and the best performing specimen with a fatigue life exceeding 750 k cycles, the SA + STEP had the overall poorest performance. This can be explained through the coarsened grains and lower sensitivity to Sv as previously described.[10] The AP + STEP fatigue results indicate a stronger dependence on Sv. In addition, as estimated in Table 2, the relatively large remnant carbide region decreased the endurance limit; however, the finer grain structure aids in dissipating localized stresses, so that AP + STEP provided better performance than the coarser grained SA + STEP specimens.

Despite previous findings that failure initiates from internal defects in L-PBF 316L stainless steel when the applied load is >275 MPa,[2] all specimens tested in this work had crack initiation sites originating from the specimen surfaces. Supplementary Figure S4 shows the fracture surface of the SR + STEP outlier, showing a large pore or keyhole adjacent to the bar surface and right at the location of crack initiation. A similar defect is noted in the fracture surface of the best performing AP + STEP specimen, although it is located away from the edge and, as shown in Figure 5a, is outside of the crack initiation zone. The worst performing AP + STEP specimen, shown in Figure 5b, exhibits a large surface notch, which is the crack initiation site. The resulting fracture is multilevel, consisting of a ridge where two crack fronts meet and along which the crack propagated. The fracture surface to the right of the crack initiation point is elevated above the surface to the left.

Figure 6 shows the fracture surface of the best performing SR + STEP specimen. The combination of lowest Sv roughness, lack of near-surface porosity or other defects, and the fine grains impeding crack proliferation results in a distinct and relatively large, stable crack propagation regime. Similar crack initiation behavior is seen in the fracture surface for the SA + STEP specimen, as shown in Figure 7a, which had the best fatigue performance of all specimens evaluated. This particular specimen also had one of the lowest Sv roughnesses and the lowest Sa roughness of all other SA + STEP bars. However, the fracture surface also reveals widespread, uniformly distributed porosity, which is not seen in the other specimen types.

Porosity reduces the fatigue life of AM metal components and, as noted for the SA + STEP specimens of this work, causes scatter and inconsistencies in the results.[33] In AM Inconel 718, there is very negligible crack propagation between internal pores during cyclic loading, with surface pores generating the dominant crack leading to failure.[34] This is observed for the poorest performing SA + STEP specimen (Fig. 7b), which shows multiple crack initiation sites—including one large near-surface inclusion—and a consequently small, stable propagation regime.

Electrochemistry

Just as fatigue life is influenced by surface roughness, the corrosion results show similar trends as E_{corr} increases with improved surface finish. Figure 8 shows CPPs, depicting this improvement for the STEP specimens. The relevant values extracted from the CPP are given in Supplementary Table S1. In Figure 8, the AP + STEP and SR + STEP have similar corrosion responses attributed to their similar microstructures with E_{corr} of $-0.670\,V_{SHE}$ and $-0.666\,V_{SHE}$, respectively. These results are similar to the approximate $-0.700\,V_{SHE}$ E_{corr} recorded by Ni et al. for polished selective laser melting 316L stainless steel.[11]

In addition to the SR specimen's decreased roughness, the smaller remnant carbide region contributes to a denser surface passive film (as indicated by the smaller i_{pass} of 0.910×10^{-5} A/cm^2). Comparatively, the SA + STEP specimen's extremely large i_{pass} ($13{,}200\times10^{-5}$ A/cm^2) is indicative of nearly no resistance between the electrolyte and

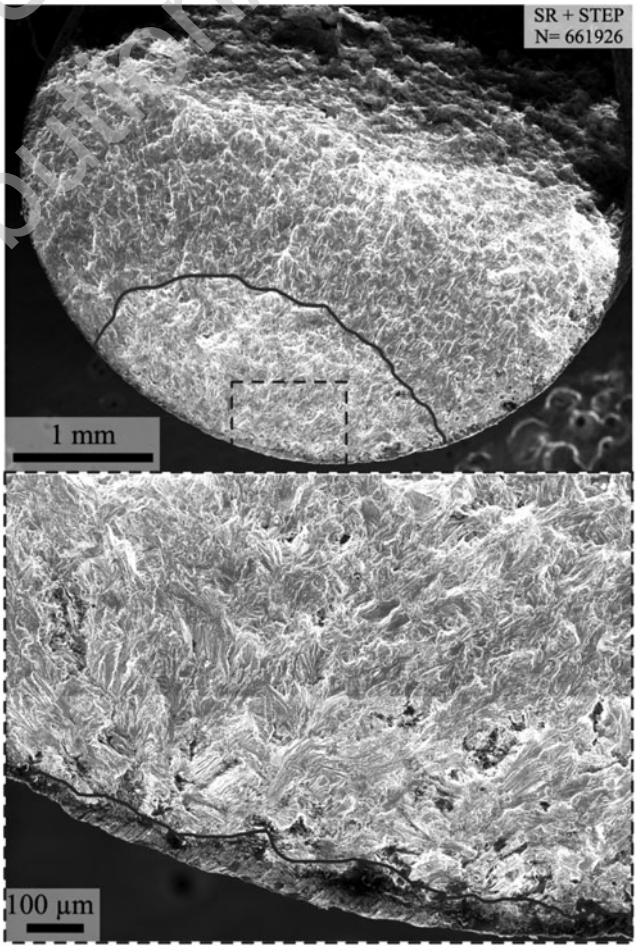

FIG. 6. A relatively large crack propagation regime is noted for the best performing SR + STEP specimen (N = 661,926 cycles). The lack of major near-surface defects and superior Sv roughness impeded formation of large crack initiation regions.

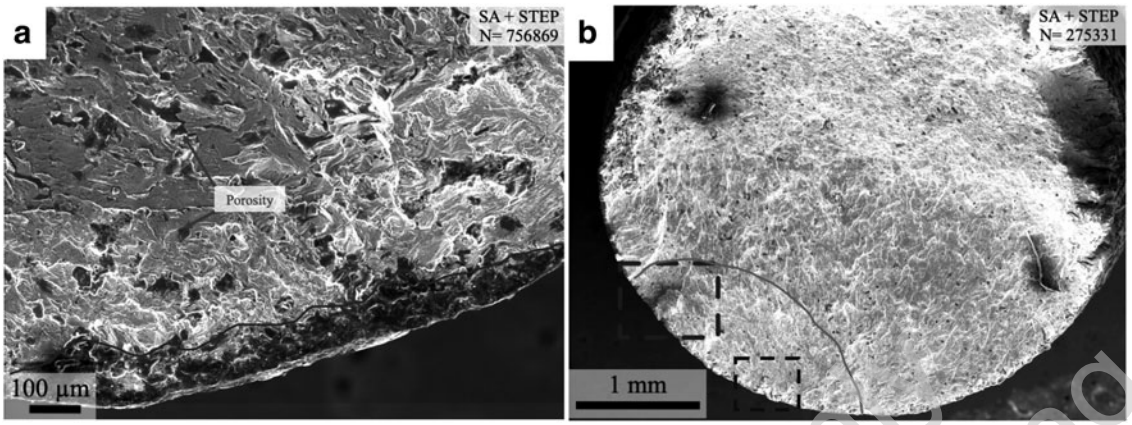

FIG. 7. The **(a)** best performing ($N = 756{,}869$ cycles) and **(b)** worst performing ($N = 275{,}331$ cycles) SA + STEP specimens showing significant porosity across the fracture surfaces. Near-surface inclusions and large surface notches were detrimental in **(b)**, while relatively low Sv and Sa roughnesses and lack of surface pores extended the fatigue life of the specimen in **(a)**.

specimen surface, and must be due to the coarser grains, the rougher surface, and prevalence of pores noted in the images of the fracture surfaces inhibiting the formation of a protective passive film. E_{bd} results ranged from approximately +0.12 to +0.20 V_{SHE}—similar to those previously measured for AM 316L having undergone some surface treatments, however not matching results of electropolished surfaces.[3]

The authors' previous evaluation of the corrosion response of L-PBF 316L stainless steel also found that a SA appreciably worsens the corrosion properties compared with AP components, decreasing E_{corr} from −0.151 to −0.537 V_{SHE}.[17] However, as parts are typically not utilized AP and commonly undergo a recrystallization heat treatment, comparison of the STEP results with those of an AP specimen is not entirely congruent.

Rather, comparison with the AP SA result would better simulate real-world applications and conditions. While the STEP does degrade the corrosion potential compared with unprocessed materials, i_{pass}, E_{pass}, and E_{bd} results are relatively similar. In addition, the very small hysteresis loops in the reverse sweeps of the CPP curves signify that pit formation and propagation are greatly impeded after the STEP. Peyre et al. similarly noted an improvement in pitting corrosion resistance postsurface smoothing modifications.[13]

The effect of a post-STEP decarburization should constitute future work. A post-STEP solution anneal under sufficient time and temperature should be undertaken in an attempt to dissolve the remnant carbides into the matrix. However, a significant increase in the steel's carbon content would impact the material properties and would constitute a substantial deviation from the original alloy of interest.

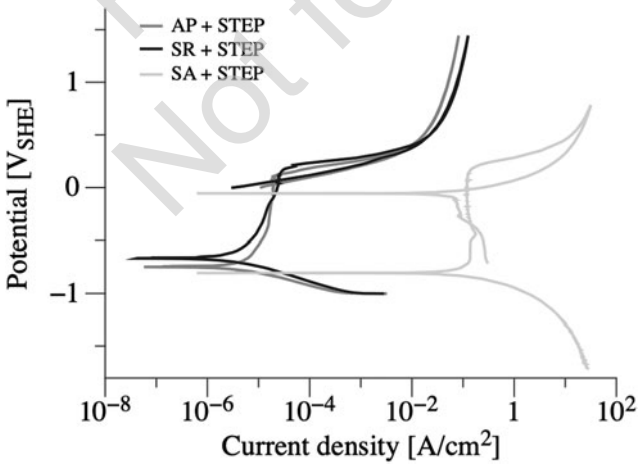

FIG. 8. CPP curves for the STEP specimens. The corrosion resistance increased with decreasing Sa surface roughness. CPP, cyclic polarization plot.

Conclusions

This work evaluated the STEP as one postprocessing technique for surface finishing L-PBF 316L stainless steel parts. Ultimately, a pre-STEP SR resulted in the optimal surface finish, which impacted both fatigue and corrosion performance. In addition to determining an optimized applied potential to decrease both the surface roughness and intergranular corrosion, the main conclusions of this work are as follows:

- A pre-STEP SR results in the smallest Sa roughness, while a pre-STEP SA decreased Sv roughness the most. While fatigue life increased with decreasing Sv, the SA + STEP specimen's coarser grained microstructure containing significant amounts of porosity eliminated any enhanced fatigue life benefits.
- The tensile strengths and endurance limits were estimated through hardness measurements. The SR + STEP had the highest estimated tensile strength, followed by the AP + STEP specimen and the SA + STEP specimen. Fatigue life results followed the similar trend with the SR + STEP specimens exhibiting the best fatigue performance and the SA + STEP specimens having the poorest performance. Under high loads, the SR + STEP fatigue life was 2–3 × greater than an AP control and 10 × greater under a lower load.
- Fractography analysis showed that all specimens failed due to crack initiation sites originating at the surfaces.

Surface defects were highly detrimental to fatigue performance.
- The STEP specimens' i_{pass} decreased and E_{corr} became more positive with decreasing surface roughness, and the STEP minimized pit formation and propagation.

Authors' Contributions

S.P. and O.H. contributed to conceptualization. S.P. provided methodology and assisted with writing—original draft preparation. S.P. and S.R. performed formal analysis and investigation. O.H. and S.R. assisted with writing—review and editing. O.H. contributed to funding acquisition, resources, and supervision.

Data Availability Statement

The raw/processed data required to reproduce these findings cannot be shared at this time due to technical or time limitations.

The authors have no relevant financial or nonfinancial interests to disclose.

Funding Information

This material is based upon work supported by the National Science Foundation under Grant No. CAREER 1944516 and the Colorado Office of Economic Development and International Trade (Grant No. CTGG1 2022-3428).

Supplementary Material

Supplementary Figure S1
Supplementary Figure S2
Supplementary Figure S3
Supplementary Figure S4
Supplementary Table S1

References

1. Gockel J, Sheridan L, Koerper B, et al. The influence of additive manufacturing processing parameters on surface roughness and fatigue life. Int J Fatigue 2019;124:380–388; doi: 10.1016/j.ijfatigue.2019.03.025.
2. Solberg K, Guan S, Razavi SMJ, et al. Fatigue of additively manufactured 316L stainless steel: The influence of porosity and surface roughness. Fatigue Fract Eng Mater Struct 2019;42(9):2043–2052; doi: 10.1111/ffe.13077.
3. Melia MA, Duran JG, Koepke JR, et al. How build angle and post-processing impact roughness and corrosion of additively manufactured 316L stainless steel. Npj Mater Degrad 2020;4(1):21; doi: 10.1038/s41529-020-00126-5.
4. Leban MB, Mikyška Č, Kosec T, et al. The effect of surface roughness on the corrosion properties of type AISI 304 stainless steel in diluted NaCl and urban rain solution. J Mater Eng Perform 2014;23(5):1695–1702; doi: 10.1007/s11665-014-0940-9.
5. Hatami S, Ma T, Vuoristo T, et al. Fatigue strength of 316 L Stainless Steel Manufactured by selective laser melting. J Mater Eng Perform 2020;29(5):3183–3194; doi: 10.1007/s11665-020-04859-x.
6. Kumar D, Idapalapati S, Wang W, et al. Effect of surface mechanical treatments on the microstructure-property-performance of engineering alloys. Materials 2019;12(16):2503; doi: 10.3390/ma12162503.
7. Cui L, Jiang F, Peng RL, et al. Dependence of microstructures on fatigue performance of polycrystals: A comparative study of conventional and additively manufactured 316L stainless steel. Int J Plast 2022;149:103172; doi: 10.1016/j.ijplas.2021.103172.
8. Wang Z, Yang S, Huang Y, et al. Microstructure and fatigue damage of 316L stainless steel manufactured by selective laser melting (SLM). Materials 2021;14(24):7544; doi: 10.3390/ma14247544.
9. Mlikota M, Dogahe K, Schmauder S, et al. Influence of the grain size on the fatigue initiation life curve. Int J Fatigue 2022;158:106562; doi: 10.1016/j.ijfatigue.2021.106562.
10. Lorenzino P, Navarro A. Grain size effects on notch sensitivity. Int J Fatigue 2015;70:205–215; doi: 10.1016/j.ijfatigue.2014.09.012.
11. Ni C, Shi Y, Liu J. Effects of inclination angle on surface roughness and corrosion properties of selective laser melted 316L stainless steel. Mater Res Express 2018;6(3):036505; doi: 10.1088/2053-1591/aaf2d3.
12. Wang S, Hu Y, Fang K, et al. Effect of surface machining on the corrosion behaviour of 316 austenitic stainless steel in simulated PWR water. Corros Sci 2017;126:104–120; doi: 10.1016/j.corsci.2017.06.019.
13. Peyre P, Scherpereel X, Berthe L, et al. Surface modifications induced in 316L steel by laser peening and shot-peening. Influence on pitting corrosion resistance. Mater Sci Eng 2000;A280:294–302.
14. Azar V, Hashemi B, Rezaee Yazdi M. The effect of shot peening on fatigue and corrosion behavior of 316L stainless steel in Ringer's solution. Surf Coat Technol 2010;204(21–22):3546–3551; doi: 10.1016/j.surfcoat.2010.04.015.
15. Menezes MR, Godoy C, Buono VTL, et al. Effect of shot peening and treatment temperature on wear and corrosion resistance of sequentially plasma treated AISI 316L steel. Surf Coat Technol 2017;309:651–662; doi: 10.1016/j.surfcoat.2016.12.037.
16. Ebrahimi M, Amini S, Mahdavi SM. The investigation of laser shock peening effects on corrosion and hardness properties of ANSI 316L stainless steel. Int J Adv Manuf Technol 2017;88(5–8):1557–1565; doi: 10.1007/s00170-016-8873-0.
17. Prochaska S, Hildreth O. Effect of chemically accelerated vibratory finishing on the corrosion behavior of laser powder bed fusion 316 L stainless steel. J Mater Process Technol 2022;305:117596; doi: 10.1016/j.jmatprotec.2022.117596.
18. Witkin DB, Patel DN, Helvajian H, et al. Surface treatment of powder-bed fusion additive manufactured metals for improved fatigue life. J Mater Eng Perform 2019;28(2):681–692; doi: 10.1007/s11665-018-3732-9.
19. Lefky CS, Zucker B, Wright D, et al. Dissolvable supports in powder bed fusion-printed stainless steel. 3D Print Addit Manuf 2017;4(1):3–11; doi: 10.1089/3dp.2016.0043.
20. Lefky C. Corrosion and Sensitized Microstructure Evolution of 3D Printed Stainless Steel 316 and Inconel 718 Dissolvable Supports. Arizona State University: Tempe, AZ, USA; 2018.
21. Hoffman R, Hinnebusch S, Raikar S, et al. Support thickness, pitch, and applied bias effects on the carbide formation, surface roughness, and material removal of additively manufactured 316 L stainless steel. JOM 2020;72:4254–4263; doi: 10.1007/s11837-020-04422-y.
22. A01 Committee. Specification for Chromium and Chromium-Nickel Stainless Steel Plate, Sheet, and Strip for Pressure Vessels and for General Applications. ASTM International; n.d. doi: 10.1520/A0240_A0240M-20.

23. E08 Committee. Practice for Conducting Force Controlled Constant Amplitude Axial Fatigue Tests of Metallic Materials. ASTM International; n.d. doi: 10.1520/E0466-15.
24. ASTM International. ASTM F3184-16, Standard Specification for Additive Manufacturing Stainless Steel Alloy (UNS S31603) with Powder Bed Fusion. ASTM International: West Conshohocken, PA, USA; 2016.
25. AMS F Corrosion Heat Resistant Alloys Committee. Heat Treatment Nickel Alloy and Cobalt Alloy Parts. SAE International; n.d. doi: 10.4271/AMS2774G.
26. ISO 25178. Geometrical Product Specifications (GPS)—Surface Texture: Areal. 2016.
27. Prochaska S, Walker M, Hildreth O. Effect of microstructure and dislocation density on material removal and surface finish of laser powder bed fusion 316L stainless steel subject to a self-terminating etching process. 3D Print Addit Manuf 2023;10(3):373–382; doi: 10.1089/3dp.2022.0190.
28. Lai W-J, Ojha A, Li Z, et al. Effect of residual stress on fatigue strength of 316L stainless steel produced by laser powder bed fusion process. Prog Addit Manuf 2021;6(3):375–383; doi: 10.1007/s40964-021-00164-8.
29. Sarkar S, Kumar CS, Nath AK. Effects of different surface modifications on the fatigue life of selective laser melted 15-5 PH stainless steel. Mater Sci Eng A 2019;762:138109; doi: 10.1016/j.msea.2019.138109.
30. Campbell FC, (ed). Elements of Metallurgy and Engineering Alloys. ASM International: Materials Park, OH, USA; 2008.
31. Davis JR, ASM International, (eds). Metals Handbook. Desk ed., 2nd ed. ASM International: Materials Park, OH, USA; 1998.
32. ISO 18265. Metallic materials—Conversion of hardness values. 2003.
33. Tammas-Williams S, Withers PJ, Todd I, et al. The influence of porosity on fatigue crack initiation in additively manufactured titanium components. Sci Rep 2017;7(1):7308; doi: 10.1038/s41598-017-06504-5.
34. Sangid MD, Ravi P, Prithivirajan V, et al. ICME approach to determining critical pore size of IN718 produced by selective laser melting. JOM 2020;72(1):465–474; doi: 10.1007/s11837-019-03910-0.

Address correspondence to:
Owen Hildreth
Department of Mechanical Engineering
Colorado School of Mines
1500 Illinois Street
Golden, CO 80401
USA

E-mail: ohildreth@mines.edu